2008-03

Real-time imaging using a 2.8 THz quantum cascade laser and uncooled infrared microbolometer camera

Behnken, Barry N.; Karunasiri, Gamani; Chamberlin, Danielle R.; Robrish, Peter R.; Faist, Jerome

Real-time imaging using a 2.8 THz quantum cascade laser and uncooled infrared microbolometer camera

Barry N. Behnken,[1,*] Gamani Karunasiri,[1] Danielle R. Chamberlin,[2] Peter R. Robrish,[2] and Jérôme Faist[3]

[1]*Department of Physics, Naval Postgraduate School, 833 Dyer Road, Monterey, California 93943, USA*
[2]*Agilent Laboratories, 5301 Stevens Creek Boulevard, Santa Clara, California 95051, USA*
[3]*Institute of Physics, University of Neuchâtel, Rue A. L. Breguet 1, 2000 Neuchâtel, Switzerland*
[*]*Corresponding author: bnbehnke@nps.edu*

Received December 5, 2007; revised January 16, 2008; accepted January 17, 2008;
posted January 29, 2008 (Doc. ID 90476); published February 20, 2008

Real-time imaging in the terahertz (THz) spectral range was achieved using a milliwatt-scale, 2.8 THz quantum cascade laser and an uncooled, 160×120 pixel microbolometer camera modified with Picarin optics. Noise equivalent temperature difference of the camera in the 1–5 THz frequency range was estimated to be at least 3 K, confirming the need for external THz illumination when imaging in this frequency regime. Despite the appearance of fringe patterns produced by multiple diffraction effects, single-frame and extended video imaging of obscured objects show high-contrast differentiation between metallic and plastic materials, supporting the viability of this imaging approach for use in future security screening applications.

OCIS codes: 110.2970, 110.6795, 140.5965.

By virtue of its unique spectral characteristics, radiation in the 0.3–10 terahertz (THz) spectral range has recently attracted attention as a promising medium for next-generation imaging technology [1–9]. Equipped with a proper illumination source and sensor, THz imaging systems are capable of standoff detection of concealed objects and of human body tissue—particularly cancerous growths, which can elude detection by traditional x-ray methods [1–3]. Such detection agility is possible because THz wavelengths are sufficiently short to provide submillimeter resolution capability, yet sufficiently long to penetrate most nonmetallic materials [4]. Furthermore, the nonionizing nature of this radiation allows for direct human exposure without the threat of ill-health effects [3]. Owing to a dearth of THz-tuned sensors and sources, however, this frequency range has not yet been fully exploited. Currently, most THz imaging systems use either antenna-coupled semiconductor detectors or cryogenically cooled bolometers operating in the scan mode. More recently, the potential use of uncooled microbolometer cameras for THz imaging using quantum-cascade laser (QCL) sources has been reported [5–9]. In this Letter, we report on the use of an uncooled, infrared microbolometer camera for imaging radiation produced by a milliwatt-scale 2.8 THz QCL.

The detection system is a commercially available, uncooled 160×120 pixel focal-plane array (FPA) microbolometer camera (IR-160, Infrared Systems) designed for passive imaging in the 8–14 μm wavelength range. With over 35% of total radiative power of the 300 K blackbody spectrum lying within this range, the device has a relatively low noise-equivalent temperature difference (NETD) at room temperature; this sensitivity allows for generation of high-quality infrared images. The pixels are constructed, using conventional microelectromechanical techniques, of a composite membrane of vanadium oxide (VO_x) and silicon nitride (Si_3N_4). When operated in the infrared regime, the camera has a dynamic range of 66 dB and NETD of less than 100 mK with $f/0.8$ optics. Since the camera is not designed for imaging at THz frequencies, sensitivity of the FPA for the 1–5 THz band of interest was separately evaluated to establish whether external illumination is required to operate the device at such frequencies. As a function of noise-equivalent power (NEP), NETD is given by [10]

$$\mathrm{NETD} = \frac{4F_{\mathrm{no}}^2}{A_{\mathrm{det}}\epsilon\pi T_l(\mathrm{d}L/\mathrm{d}T)}\mathrm{NEP}, \tag{1}$$

where F_{no} is the f number of the optics used for focusing the beam onto the FPA, A_{det} is the area of a single pixel, ϵ is the emissivity of the membrane material, and T_l is the lens transmissivity. L, the spectral irradiance of the source, is given by [11]

$$L(T) = \frac{\epsilon_t P(T)}{\pi}, \tag{2}$$

where ϵ_t is the emissivity of the illumination source and $P(T)$ is the exitance of the source in the THz frequency range of interest. Using Planck's radiation law and the fact that, at 300 K, $h\nu < kT$ for the 1–5 THz range [11],

$$P(T) \approx \int_0^{\nu_c} \frac{2\pi kT}{c^2}\nu^2\mathrm{d}\nu \approx \frac{2\pi kT}{3c^2}\nu_c^3, \tag{3}$$

where ν_c is the high-frequency cutoff of the THz region (5 THz). This formula yields a total incident power density over the 1–5 THz region of approxi-

mately 12 W/m^2 at 300 K—significantly less than that associated with the 8–14 μm wavelength range ($\sim$170 W/m^2). Thus the NETD of the detector in the THz regime can be succinctly expressed as

$$\mathrm{NETD} = \frac{6c^2F_{\mathrm{no}}^2}{A_{\mathrm{det}}\epsilon\pi T_l k \epsilon_t v_c^3}\mathrm{NEP}. \quad (4)$$

The microbolometer camera used in the present study employs an $f/1$ lens with $A_{\mathrm{det}}=50\times50$ μm^2. With the QCL source exhibiting blackbody characteristics, ϵ_t can be taken to be unity. NEP is evaluated by first considering the various sources of noise within the detector. In microbolometers, the predominant noise source at lower readout bias currents is Johnson's [10]. At room temperature, the rms voltage of this noise contribution is given by [11]

$$V_{JN} = [4k_BTR\Delta f]^{1/2} = 7.0\ \mu\mathrm{V}, \quad (5)$$

where $R=10$ kΩ is the equivalent resistance for noise analysis when the microbolometer and 20 kΩ load resistor are serially connected in the readout circuit [10]. The frequency bandwidth, $\Delta f=0.29$ MHz, is obtained from the 30 Hz frame rate at which the FPA's 160×120 pixel array is individually sampled. It follows that detector NEP, given by the ratio of V_{JN} to detector responsivity, $\mathcal{R}_v=2\times10^5$ V/W [12], is approximately 35 pW.

As a result of optical modifications intended to maximize the amount of THz radiation received by the FPA, two of the optical parameters in Eq. (4) (T_l,F_{no}) differ from those for the original system. Early experiments using the camera's stock germanium (Ge) lens indicated that the incident THz beam was strongly attenuated by antireflection coatings applied to the lens; to correct this deficiency, the Ge lens was replaced with a 1 inch (2.54 cm) diameter, 20 mm focal length bi-convex $f/1$ lens made of Picarin (PPL-1″—20 mm–BC, Microtech Instruments). For focusing of the incident collimated beam, the lens was mounted 20 mm from the FPA, yielding an effective camera field of view of 53°. Picarin, measured to have a transmissivity (T_l) of 0.65 at 2.8 THz, was also used as the source material for the 2 inch (5.08 cm) diameter, 4 mm thick cryostat window. The emissivity metric ϵ, which is directly proportional to the membrane's absorption of incident radiation, has not been well characterized for THz frequencies. By using infrared emissivity values, however, one can obtain an upper limit of detector performance and establish whether external illumination is necessary under the most liberal of assumptions. Using $\epsilon=0.8$ (a well-documented value for the 8–14 μm wavelength range [10]), the NETD of the microbolometer is found to be approximately 3 K. This result, which is more than 1 order of magnitude higher than the commercially specified NETD of the camera for passive infrared imaging (0.1 K), confirms the need for external illumination when using the microbolometer camera at THz frequencies.

The QCL used in these experiments, fabricated via molecular beam epitaxy on a semi-insulating GaAs substrate using a bound-to-continuum transition design, consists of a 14 μm multiple quantum well (MQW) active region comprised of 120 periods [12]. Owing to asymmetric diffraction effects that are produced by the active facet's rectangular (14 μm $\times$200 μm) cross section, the beam propagates with greater divergence along the vertical than the lateral dimension, yielding an elliptical beam shape. To mitigate heating in the active region, the laser was nominally operated at a 300 kHz repetition rate with a 0.9–1.6 A current bias and 8–15% duty cycle. The resulting ranges of peak and average output power from the QCL were 5–9 mW and 0.4–1.4 mW, respectively. Current-versus-voltage measurements indicated that QCL dynamic impedance during lasing is about 3.4 Ω; impedance matching to the 50 Ω pulse generator was accomplished by incorporating a step-down transformer into the electrical circuit. To accommodate the laser's stringent cooling requirements, the QCL was attached to a copper-based mount (to promote energy dissipation through thermal conduction) and cooled to 10 K using closed-cycle refrigeration. To maximize transmission of the highly divergent QCL beam from the cryostat, the laser carrier was positioned immediately adjacent to the window interior (within 13 mm). External to the cryostat were placed a pair of gold-plated, 90° off-axis parabolic (OAP) reflectors ($f/1$ and $f/2$, each 50.8 mm in diameter) for collimating the beam and steering it toward the camera. The $f/2$ OAP was displaced 25 mm from the $f/1$ OAP, which was positioned 32 mm from the cryostat window. The camera's Picarin lens was positioned approximately 90 mm from the $f/2$ OAP.

Imaging experiments were performed by inserting metallic objects, wrapped within various obscurants (plastic, paper, and cloth), roughly midway between the two parabolic mirrors such that a focused image fell on the microbolometer FPA. For single-frame imaging, the laser was typically operated at a 300 kHz repetition rate, a bias of 1.3–1.6 A, and 15% duty cycle. Figure 1 is representative of the results obtained and demonstrates the methodology used to refine the image quality of a utility-knife blade wrapped in opaque plastic tape [Fig. 1(a)]. Although single-frame images showed good contrast between the two objects [Fig. 1(b)], further improvements were achieved by taking multiple individual images of the stationary ensemble. When image-averaging techniques are used to combine these frames into a composite image [Fig. 1(c)], noise effects are averaged out and overall clarity is improved. Finally, using noise-reduction software applications, still greater contrast can be achieved [Fig. 1(d)]. The advantage offered by image averaging and/or computer-based postprocessing techniques is perhaps best appreciated by noting the small speck of (nonmetallic) foreign material that became accidentally embedded within the plastic tape (visible in THz images near the top of the illumination region). In the unmodified single-frame THz image [Fig. 1(b)], the contaminant is barely distinguishable within the image's background noise. In Figs. 1(c) and 1(d), however, it is clearly recognizable as a distinct object. Given the

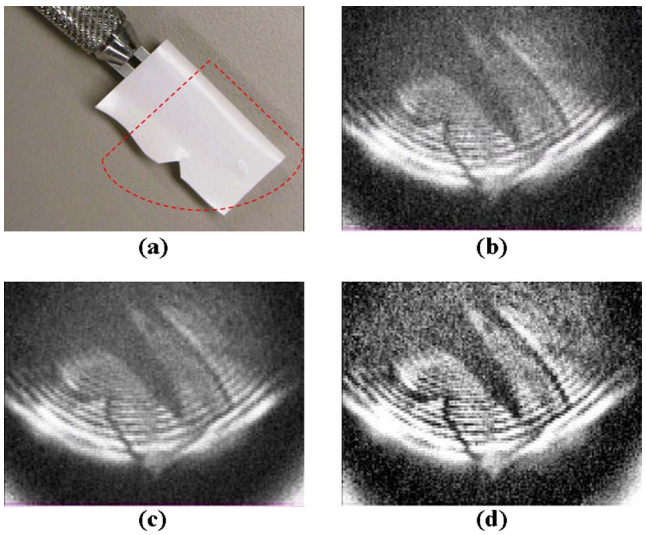

Fig. 1. (Color online) Imaging of a small utility-knife blade wrapped in opaque plastic tape. (a) Conventional digital photograph. Dotted region represents approximate area of illumination. (b) Single-frame image of blade assembly illuminated with 2.8 THz QCL radiation and imaged with microbolometer camera. (c) Image generated by computationally averaging 50 individual frames. (d) Fifty-frame composite image, refined using MATLAB image-processing utility software.

large current densities required for lasing, a principal limiting factor associated with prolonged imaging is thermal population of the laser's quantized energy states via Joule heating of the QCL. To minimize laser heating during extended (video) imaging, bias current and duty cycle were decreased to roughly 930 mA and 8%, respectively. Despite the resulting reduction in average laser power, real-time video recordings under these operating parameters are only slightly inferior to still-frame images (Fig. 2). Significant diffraction effects, produced by the influence of various system optics on the THz beam (QCL aperture diffraction, as well as etalon effects arising within the Picarin lens and cryostat window), are apparent in the form of sharply defined, concentric fringe patterns appearing throughout each of the THz images.

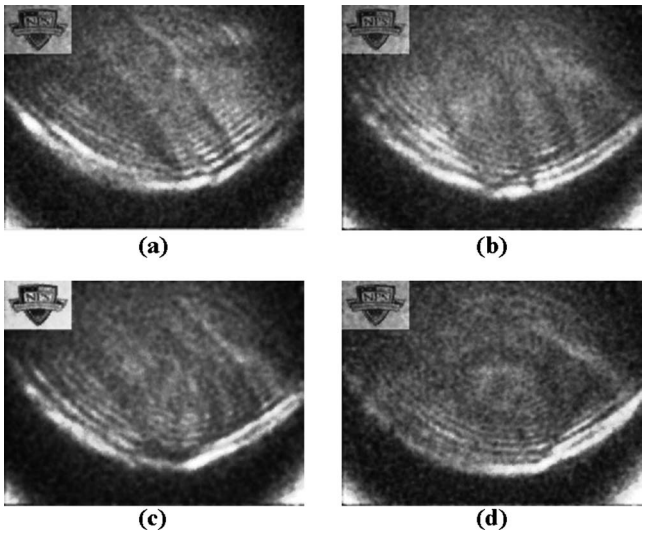

Fig. 2. (Multimedia online) Single-frame excerpts from video recordings of metallic objects concealed by opaque plastic tape. (a) Utility blade from Fig. 1 (698 KB). (b) Dentist's pick (870 KB). (c) Paper clip (783 KB). (d) Plastic/wire tie twisted into the shape of a loop (673 KB)

In summary, we have demonstrated the ability to image metallic objects obscured by opaque materials using 2.8 THz radiation and a commercially available microbolometer camera. These results confirm that microbolometer pixel membranes remain absorptive well beyond the 8–14 μm wavelength range, and that uncooled microbolometer cameras hold promise as an inexpensive, compact platform for THz imaging under certain scenarios. Calculations indicate that camera NETD in the 1–5 THz frequency range is at least 3 K, confirming the need for external radiation sources when imaging with microbolometer FPAs in this regime. Improvements upon this imaging scenario are currently being investigated.

The authors thank Scott Davis and Don Walters at NPS for helpful discussions and Sam Barone for technical help in fabricating the step-down transformer. This work is supported by the Air Force Office of Scientific Research (AFOSR).

References

1. D. A. Zimdars and J. S. White, Proc. SPIE **5411**, 78 (2004).
2. J. F. Federici, D. Gary, R. Barat, and D. Zimdars, Proc. SPIE **5781**, 75 (2005).
3. K. Humphreys, J. P. Loughran, M. Gradziel, W. Lanigan, T. Ward, J. A. Murphy, and C. O'Sullivan, in *Proceedings of the 26th Annual International Conference of the IEEE* (IEEE, 2004), pp. 1302–1305.
4. J. E. Bjarnason, T. L. J. Chan, A. W. M. Lee, M. A. Celis, and E. R. Brown, Appl. Phys. Lett. **85**, 519 (2004).
5. G. Karunasiri, presented at the 7th International Conference on Technology and the Mine Problem, Monterey, Calif., 2–4 May 2006.
6. A. W. M. Lee and Q. Hu, Opt. Lett. **30**, 2563 (2005).
7. A. W. M. Lee, B. S. Williams, Q. Hu, and J. L. Reno, IEEE Photonics Technol. Lett. **18**, 1415 (2006).
8. B. N. Behnken, M. Lowe, G. Karunasiri, D. Chamberlin, P. R. Robrish, and J. Faist, Proc. SPIE **6549**, 65490C (2007).
9. B. N. Behnken, G. Karunasiri, D. Chamberlin, P. R. Robrish, and J. Faist, in *Proceedings of the Ninth International Conference on Intersubband Transitions in Quantum Wells*, D. Indjin, Z. Ikonic, P. Harrison, and R. W. Kelsall, eds. (University of Leeds, UK, 2007).
10. R. A. Wood, in *Semiconductors and Semimetals*, Vol. 47, pp. 43–121 (1997).
11. E. L. Dereniak and S. D. Boreman, *Infrared Detectors and Systems* (Wiley, 1996).
12. J. Faist, L. Ajili, G. Scalari, M. Giovannini, M. Beck, M. Rochat, H. Beere, A. G. Davies, E. H. Linfield, and D. Ritchie, Philos. Trans. R. Soc. London **362**, 215 (2003).